

Caleb Graham¹ & Ruben E. Perez²

¹Research Assistant, Department of Mechanical and Aerospace Engineering, Royal Military College of Canada, Kingston, ON, K7K 7B4, Canada

²Professor, Department of Mechanical and Aerospace Engineering, Royal Military College of Canada, Kingston, ON, K7K 7B4, Canada

Abstract

This paper investigates the aerodynamic effects of externally mounted liquid hydrogen tanks. These tanks are much larger than traditional engine nacelles and so pose new challenges in their design and integration. The trends in the interference drag between the tanks and the DLR-F6, a representative transport aircraft, are quantified by a computational fluid analysis. A model is developed for integration with conceptual design codes. Results show shorter, large diameter tanks can reduce the tank-wing interference drag. In addition, results suggest some configurations could lower overall drag, offsetting the penalty of externally mounted fuel tanks.

Keywords: Aerodynamics, Liquid Hydrogen, Aircraft Design, Design Synthesis

1. Introduction

Over the past few decades environmental factors have driven the design and operation of long range transport aircraft towards reducing their green house gas emissions. The pledge by the International Civil Aviation Organization (ICAO) in 2022, and of similar organizations over the last several years, to hit net zero green house emissions by 2050 has placed further emphasis on environmental factors during the design and operation of new medium and long range transport aircraft [1]. From 2009-2019, through increases in efficiency, the industry reduced emissions by 21.5% per passenger per kilometer [2]. However, with demand expected to increase by 2.7-3.5% per year until 2050 [2], incremental gains in efficiency won't be enough to reach the industry's net zero goal. To reach ICAO's goal, more intensive decarbonisation efforts will be required.

Alternate fuels are considered by many to be a necessary step to reaching net zero targets. While research is being done on possible alternatives, including liquid methane, and synthetic aviation fuels, liquid hydrogen (LH2) has emerged as a commonly suggested solution, with industry leaders such as Airbus beginning development of their own hydrogen powered aircraft [3]. Thanks to it's high specific energy, research on LH2 as an aviation fuel goes back to the early 1900's, however it was never adopted owing to its low density, high cost compared to alternatives, and the difficulties storing and handling it [4]. Today, with the rising cost of kerosene, and the need to reach emissions targets, liquid hydrogen has seen a resurgence thanks to its lower NO_x , and non existent CO_2 emissions [5]. While LH2 powered aircraft do emit more water vapour than their kerosene powered counterparts, the effect of these emissions would be insignificant compared to the CO_2 emissions that would be eliminated [6]. Integrating liquid hydrogen is not without challenge however, with the fuel's requirement to be stored cryogenically, as well as it taking up four times the volume of kerosene [4], finding a way to store enough fuel for long distance flights has become a major problem. While many configurations have been explored, most involve storing the fuel in the fuselage [3, 7]. A common layout uses a tank in the aft section of the fuselage, while this comes at the advantage of being a convenient location

to integrate the tank(s), with a reduced drag penalty, it also requires space that would otherwise be used for passengers or cargo. Storing fuel this way also poses problems for stability and flight dynamics as the center of gravity shifts during flight. This problem is exacerbated for larger aircraft, and coupled with the economic challenges of reducing the amount of passengers, or cargo, per flight, and the higher cost of hydrogen fuel [5], studies tend to disagree on the feasibility of the approach for anything other than regional aircraft [7]. We must also consider the potential regulatory issues with storing large volumes of cryogenic fluid next to passengers.

Rather than contend with the challenges posed by integrating liquid hydrogen tanks into the fuselage, this research explores the aerodynamic effects of mounting the fuel tanks externally. This configuration has the potential to scale better to larger aircraft and could allow for easier maintenance of the liquid hydrogen tanks, while avoiding the potential economic, regulatory, and design challenges with internal fuel tanks. This approach is not new, in 1955 NACA tested the feasibility of hydrogen powered aircraft using a modified B-57 with tanks mounted beneath the wing tips, while the test flights were successful the project ultimately wasn't pursued further [8]. More recently, in 2019 Silberhorn et al. investigated hydrogen tank integration of several tank concepts. The group identified the underwing mounted tank as a possibility, and while the drag penalty of this concept is a major factor they determined it was a feasible option [9]. Similarly in 2023, Thomas et al. explored a liquid hydrogen aircraft with either internal or external fuel tanks. The drag penalty of the external tanks was identified as a constraint, though analysis was limited. [10]. Given the potential advantages, the external fuel tank configuration merits a more thorough investigation of, what may be its largest downside, its drag penalty. This study aims to characterize the drag caused by these external fuel tanks. While the drag of similar devices has been explored before, mainly in the form of engine nacelles, [11][12] the fuel tanks that will be required for LH2 aviation will likely be significantly larger and will have different shapes than the devices that have been researched in the past. This necessitates further investigation of these tanks. Additionally, the focus of this research is on the interference caused by the tank-wing interaction rather than on the tanks themselves. The goal is to create a model which can be used to estimate the interference drag of these tanks, which could be used for conceptual design or be integrated into existing design codes.

2. Methodology

To investigate the interference drag of the tank-wing interaction, a wide range of conditions need to be tested, both to be able to analyze the trends as well as to create an analytical model that can predict the interference drag. To this end a canonical aircraft, representative of a long range transport, was used. In addition, tank geometries of varying size and position will be need to be generated. This section details the aircraft model used in this study, the parametric tank model, and presents details on the use and accuracy of the solver that will be used for the computational fluid analysis performed in this study.

2.1 Base Aircraft

This study will use the DLR-F6 geometry from the 2^{nd} NASA Drag Prediction Workshop. The DLR-F6 is a model made to be representative of a generic transport aircraft designed for transonic flight. A schematic of the aircraft is shown in Figure 1, the plane has a quarter chord sweep of 25 degrees and a dihedral of 4.787 degrees, its mean aerodynamic chord (MAC) is 141.2 mm and its reference area is 72700.0 mm². A schematic of the wing is shown in Figure 2, the wing is made up of 4 airfoil sections, section 1 uses an Ha5 profile, sections 2-4 use an R4 profile, it has an aspect ratio of 9.5 and a taper of 0.3, its projected half span (b/2) is 585.7mm. This aircraft was chosen as it has a known, publicly available geometry, as well as wind tunnel measurements which provide a means to validate the initial aerodynamic analysis of the F6. For the purposes of this research the tank-nacelle interference is not of interest, so for simplicity the aircraft will be modeled without pylons and engine nacelles.

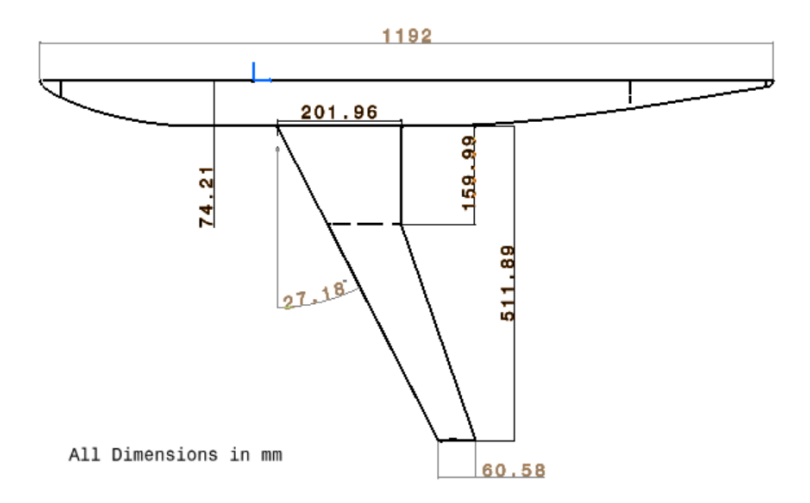


Figure 1 – DLR-F6 geometry [13]

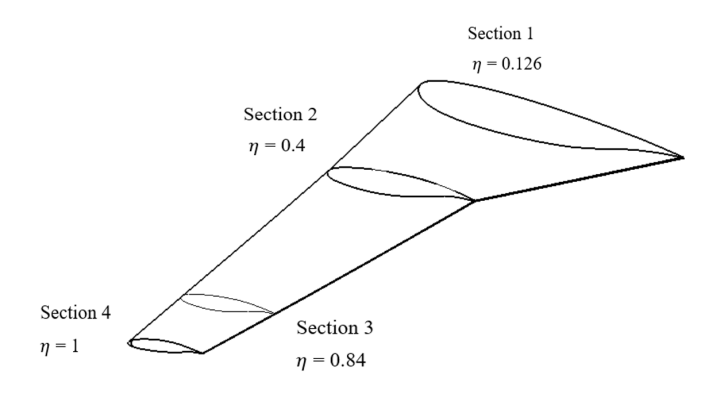


Figure 2 – DLR-F6 wing profile [13]

2.2 Fuel Tanks

Fuel tank geometries are parametrically generated and integrated with the DLR-F6 for analysis. For simplicity the tanks will be modeled without pylons, while drag would be expected to be higher with a pylon, Stańkowski *et al.* showed the difference to be small, 6 drag counts (dc) or less depending on angle of attack (AoA), for similar flow conditions to the ones in this study [11]. The tanks are cylindrical with the forward end using a spherically blunted tangent ogive profile, and the rear end using a tangent ogive profile. Ogive lengths are determined based on the user defined tank diameter, and on user defined length/diameter ratios for the forward and aft surfaces. Ogive radii (ρ) are determined using Equation 1, where L is the ogive length and R is the tank radius [14]. The length of the cylindrical section is the difference between the user defined total tank length, and the two ogive lengths. For changing tank positions, a tank origin is defined as some coordinate in space, relative to the DLR-F6, which the rest of the tank is referenced to.

The tank is generated as an axis symmetric body of revolution. The profile is made up of three sections. The aft section is defined as an arc segment with radius equal to the aft ogive radius, and origin offset from the tank origin by half the length of the cylindrical section in the x direction, and by the difference between the ogive radius and tank radius in the y direction. The arc is between two points, one at y=0, and the other at the tangent point between the aft and cylindrical sections. The front section is further subdivided into two sections, the ogive portion and the spherical portion. The ogive portion is defined similarly to the rear section, however the arc is from the tangent point between the front ogive section and the cylindrical section, to the tangent point between the front ogive section and the spherical section. The tangent point for the spherical section was determined

using equations 2 and 3 [14]. The spherical nose is defined as an arc segment with radius (r_n) set by the user, and origin offset from the front ogive origin by equation 4 in the x direction [14]. The arc is from the tangent point between the front ogive and the spherical section, to the point at y = 0. Each section is made up of 25 points, equally spaced on their respective profiles. The cylindrical section is a line at $y = tank \ radius$ between the front and rear ogive sections. The line is defined using the end points of the ogive sections. A section view of a sample tank geometry is shown in Figure 3 with the key points highlighted.

$$\rho = \frac{R^2 + L^2}{2R} \tag{1}$$

$$y_t = \frac{r_n(\rho - R)}{\rho - r_n} \tag{2}$$

$$x_t = x_o - \sqrt{r_n^2 - y_t^2} (3)$$

$$x_0 = L - \sqrt{(\rho - r_n)^2 - (\rho - R)^2}$$
 (4)

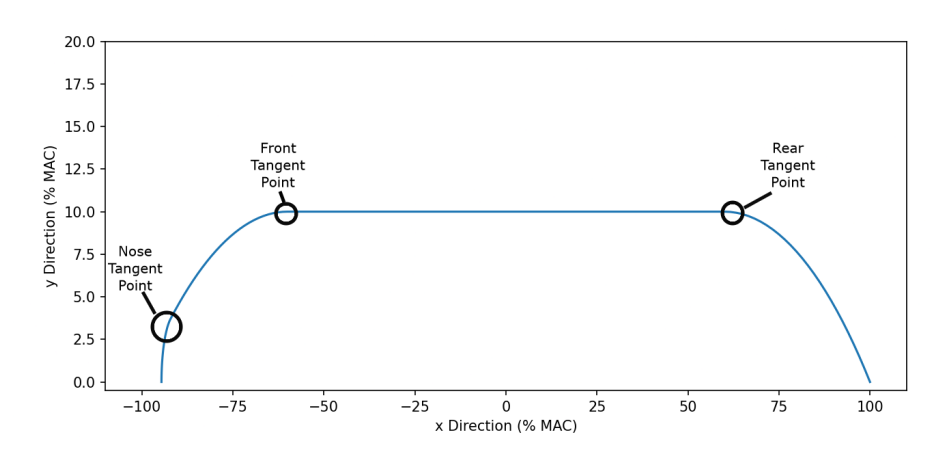


Figure 3 – Section view of sample tank geometry

For the purposes of this study, a wide range of tank sizes and positions need to be investigated. Geometries ranging from 20% mean aerodynamic chord (MAC) to 60% MAC in diameter and 250% MAC to 350% MAC in length are generated. These tank sizes are intended to cover a wide range of scenarios, from a hybrid setup using a mix of internal and smaller external fuel tanks, to setups requiring large volume external tanks, which may be necessary for long distance flights or if tanks require thick insulation. Each size tank will be tested in a wide range of positions relative to the base aircraft. The positions are defined by normalized parameters, with ξ representing the normalized chordwise position of the tank, given by Equation 5, where c represents the wing chord, x represents the axial position of the tank origin, and X_{LE} represents the x position of the leading edge of the wing. η represents the normalized spanwise position of the tank, given by Equation 6, where y represents the spanwise position of the tank origin, and b/2 represents the half span of the aircraft. κ represents the distance in the z direction between the wing center (z_{wing}) and the tank surface (z_{Tank}) , normalized by MAC, given by Equation 7. Each configuration will be run at angles of attack from -2° to 2° and for Mach numbers between 0.35 and 0.75. A full list of test parameters is shown in Table 1, every possible combination of parameters will be tested. Figure 4 shows every tank size being investigated at position $(0.5\xi, 0.2\eta, -0.2\kappa)$.

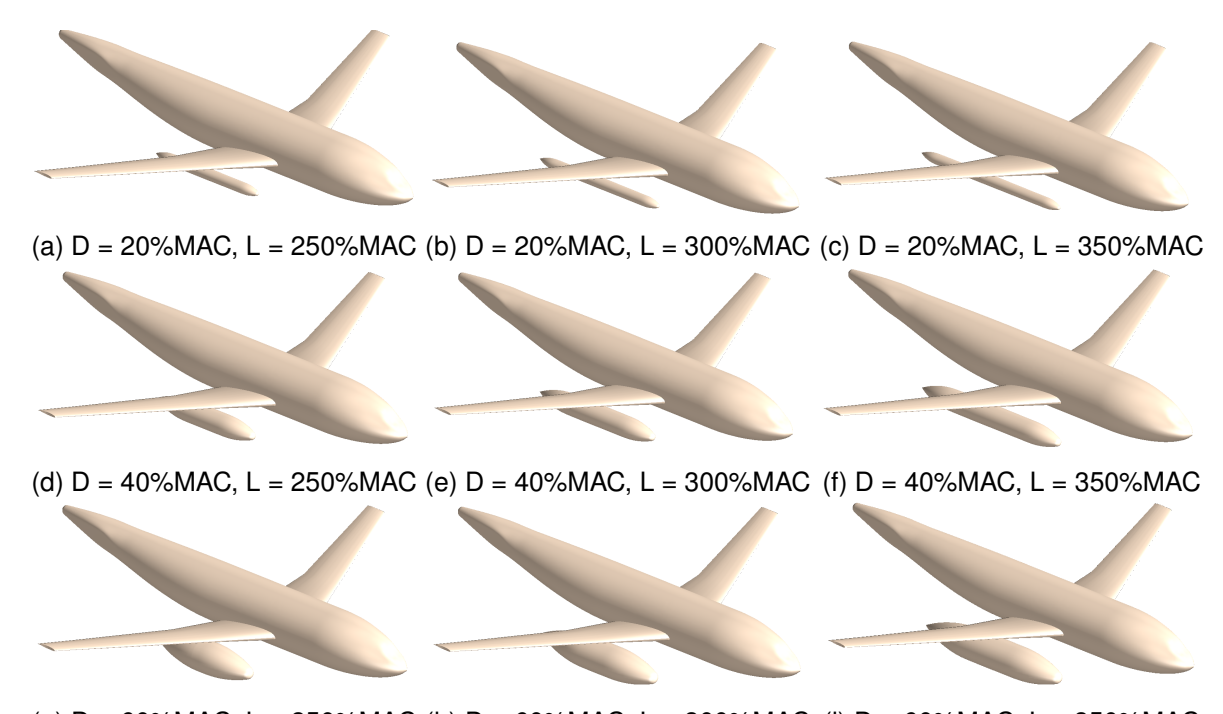
$$\xi = \frac{x - x_{LE}(\eta)}{c(\eta)} \tag{5}$$

$$\eta = \frac{y}{b/2} \tag{6}$$

$$\kappa = \frac{z_{Wing}(\eta) - z_{Tank}}{MAC} \tag{7}$$

Table 1 – Parametric Analysis Test Cases

Length (%MAC)	Diameter (%MAC)	Velocity (Mach)	AoA (Angle)	ξ	η	κ
250	20	0.35	-4	0.2	0.2	0.1
300	40	0.55	-2	0.3	0.4	0.15
350	60	0.75	0	0.4	0.5	0.2
			2	0.5	0.6	0.25
				0.6	8.0	0.3



(g) D = 60%MAC, L = 250%MAC (h) D = 60%MAC, L = 300%MAC (i) D = 60%MAC, L = 350%MAC

Figure 4 - Tank sizes to be tested

2.3 Solver and Simulation Setup

Flightstream is the solver that will be used for this study. Flighstream is a surface vorticity flow solver which has been validated against wind tunnel data for similar flow conditions to the ones in this study and has been shown to be reasonably accurate [12]. The software is also capable of automatically generating a watertight mesh when using its native file format, this mesh will be used for all simulations. An image of the simulation set up is shown in Figure 5. The DLR-F6 geometry is a half-model which is mirrored for the simulation, likewise the single tank simulations are also mirrored. The steady state solver is used with a constant free stream velocity. Viscous coupling and compressible flow were also enabled. In addition, a transitional turbulent boundary layer is used with a standard smooth surface. The exact workings of the solver can be found in reference [15].

Using the solver the coefficient of drag (C_D) and coefficient of lift (C_L) is first determined for the base aircraft for every combination of AoA and velocity. A template is made from this simulation that will be copied for all other runs. Next, a tank is generated for every combination of position, diameter, and length. Each tank is simulated both by itself, and after being integrated with the DLR-F6, for every combination of AoA and velocity.

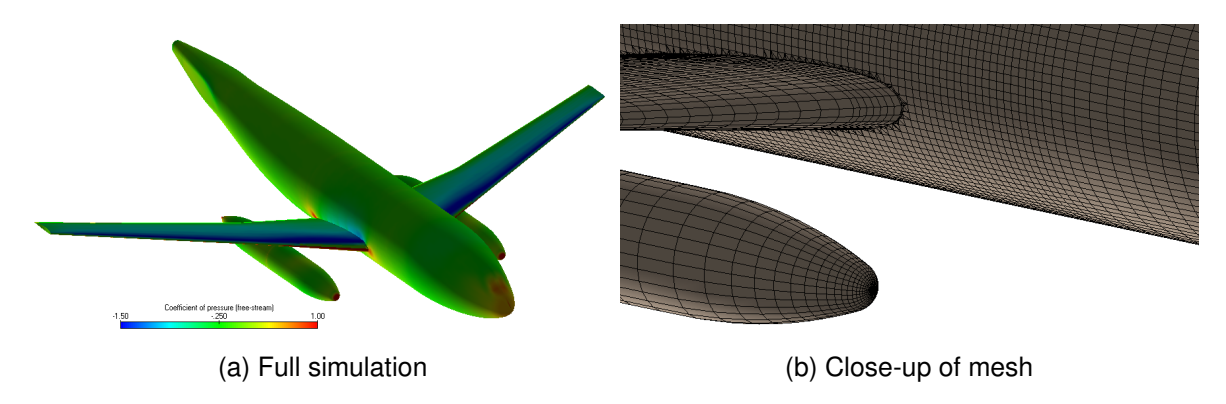


Figure 5 – Simulation setup of DLR-F6 with fuel tank

2.4 Validation

For validation the C_D and C_L are determined, using the solver, for angles of attack from -5° to 2° at Mach 0.75, the results are compared to data from the NASA NTF and ONERA S2MA wind tunnels [16]. To better match the conditions in the wind tunnel, which used trip dots on the leading edge of the wing, the boundary layer was set to turbulent for the validation [16]. A plot of C_L against AoA and C_L against C_D of the DLR-F6 as determined by both the NASA NTF and ONERA S2MA wind tunnels is shown in Figure 6, with the addition of the flow solver solution [16]. The solver solution matches the experimental data well, it overpredicts C_L by 0.007 on average and C_D by 0.6 drag counts on average, compared to the ONERA data. In addition, the slope of the C_L AoA curve determined by the solver appears to match the slope of the curve determined in the wind tunnel. Based on this, the changes in drag between different tank geometries are expected to be accurate, and the absolute drag values are expected to be close to the real world values.

2.5 Post Processing

The tank-wing interference drag is determined for each test case based on the drag of the base aircraft, the isolated tank, and the combined geometries, using Equation 8. During testing it was found that the addition of the tanks was also affecting the C_L , and hence the induced drag (C_{Di}) . The tanks were seen to affect the load distribution of the wing, therefore changing the Oswald efficiency number (e). The largest change in e was 0.035. Due to computational limitations, matching C_L between the baseline and each run was impractical, therefore only the parasitic drag (C_{D0}) will be used in determining interference drag. For readability C_D will be scaled into drag counts by multiplying by 10000.

$$C_{D0 interference} = C_{D0 Combined Geometry} - (C_{D0 BaseAircraft} + C_{D0 Isolated Tank})$$
(8)

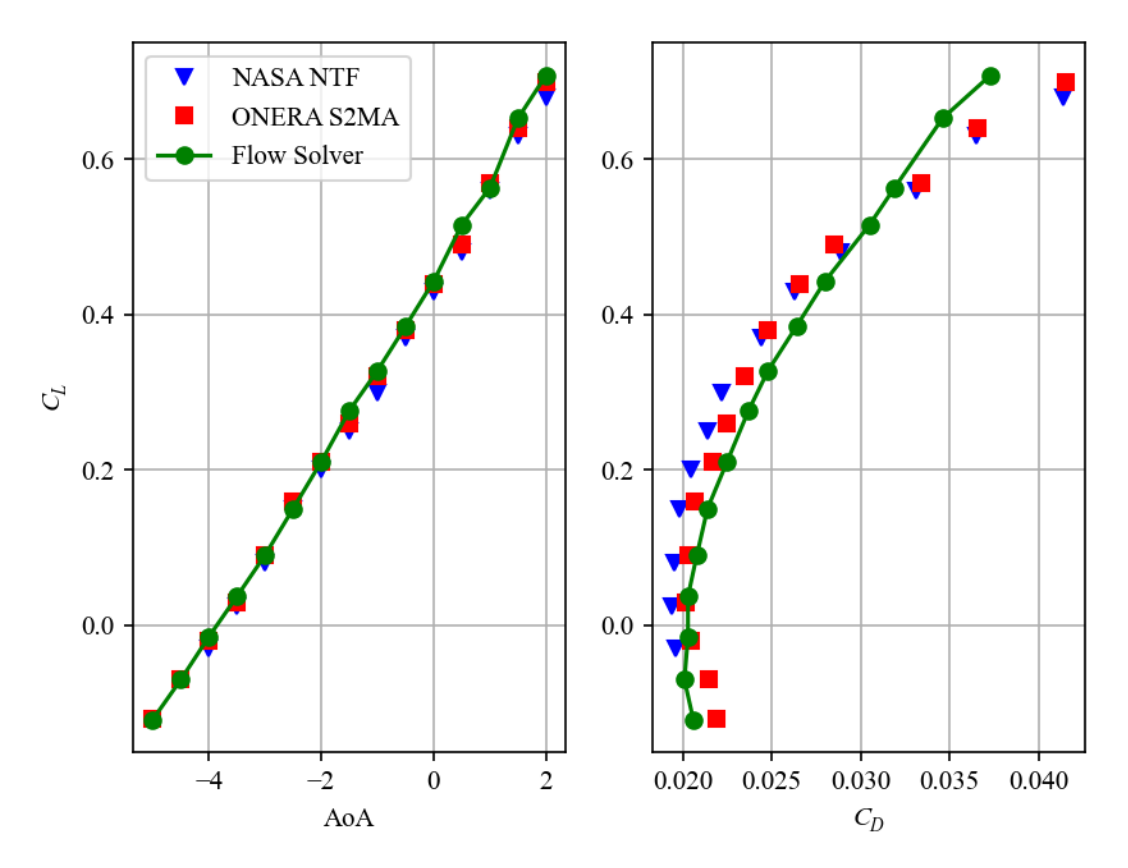


Figure 6 - Flow solver validation

3. Results

The test cases were analyzed to determine which factors are affecting the tank-wing interference drag. With the trends understood, a model was fit to the data using a least squares optimization.

3.1 Test Cases

The data was grouped into runs where all parameters except for AoA and velocity were held constant. The interference drag was plotted against angle of attack at each velocity. An example is shown in Figure 7 for position $(0.5\xi,\,0.2\eta,\,-0.2\kappa)$ with length 350% MAC and diameter 20% MAC. The tanks behave as expected, interference drag increases with increasing AoA. However, interference drag was highest at Mach 0.55 for the majority of test cases. It was found that at Mach 0.55 and 0.75 the boundary layer on the fuel tanks transitioned much earlier than at Mach 0.35. In addition, due to the lower Reynolds number the boundary layer is thicker at Mach 0.55 than at Mach 0.75. It's believed that the thicker boundary layer causes the interference drag to be higher at Mach 0.55.

The effect of chordwise position was also explored. The interference drag is shown as a function of chordwise position in Figure 8, at 0.2 η , -0.2 κ , a diameter of 20% MAC, and length of 250% MAC. The AoA is 0 and velocity is Mach 0.75. The results show little change in interference drag with chordwise position. The largest difference is 2 drag counts, which is believed to be within the margin of error of the solver.

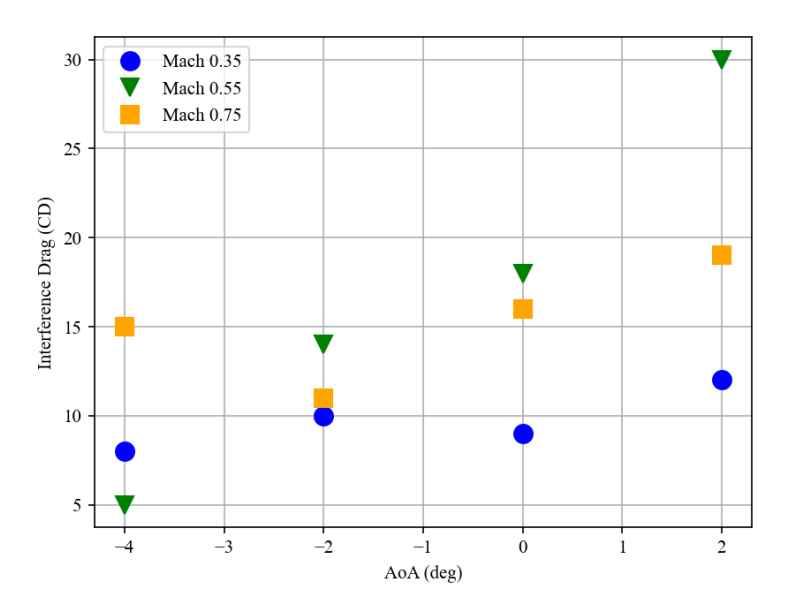


Figure 7 – Interference drag against angle of attack

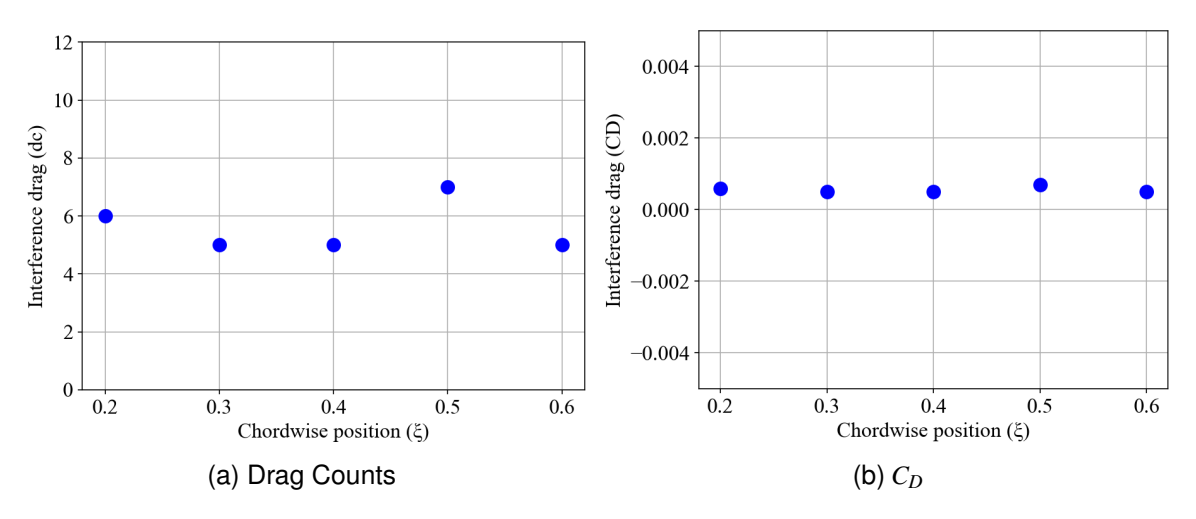


Figure 8 – Interference drag against chordwise position

Similarly, data was grouped into runs where all parameters except for length and diameter were held constant. The interference drag was plotted against length for each diameter, Figure 9 shows such a plot for position $(0.5\xi,\,0.2\eta,\,-0.2\kappa)$, at an AoA of 0° and Mach 0.75. There are several factors affecting the results here. In general interference drag increases with increasing length and decreases with increasing diameter. This suggest interference drag is related to fineness ratio, which will be defined as the length of the tank over the diameter of the tank. Table 2 however, shows that interference drag is not strictly a function of this ratio, the absolute length and diameter are still important. It was found that tanks with a higher fineness ratio have an earlier boundary layer transition, compared to the overall length of the tank. This can be seen in a comparison between the shape factor of a high and low fineness ratio tank, as shown in Figure 10. In addition, longer tanks lead to more boundary layer growth. As seen previously, a thicker boundary layer over the tanks tends to increase interference drag, and therefore, interference drag tends to increase both with length and with fineness ratio.

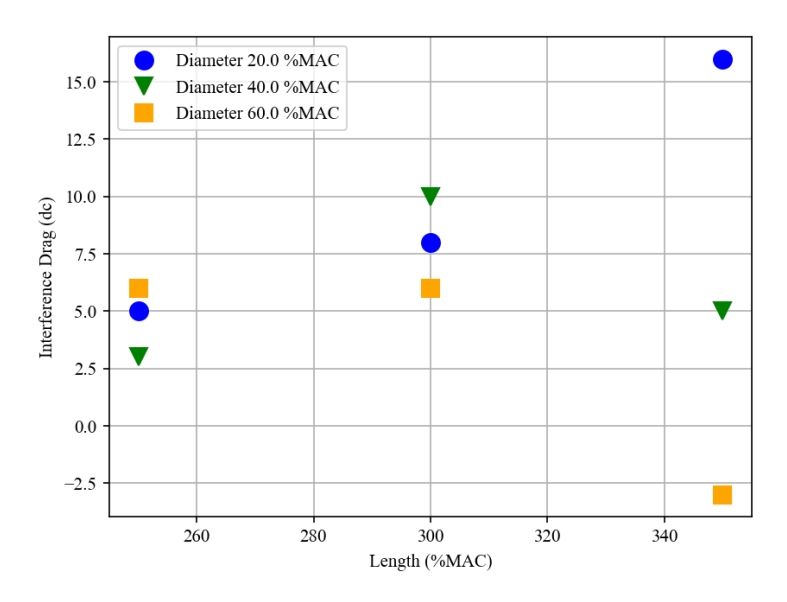


Figure 9 – Interference drag against length

Table 2 – Interference drag for different sized tanks with the same fineness ratio

Diameter (%MAC)	Length (%MAC)	L/D	Interference (dc)
25	250	10	3
30	300	10	10
35	350	10	12

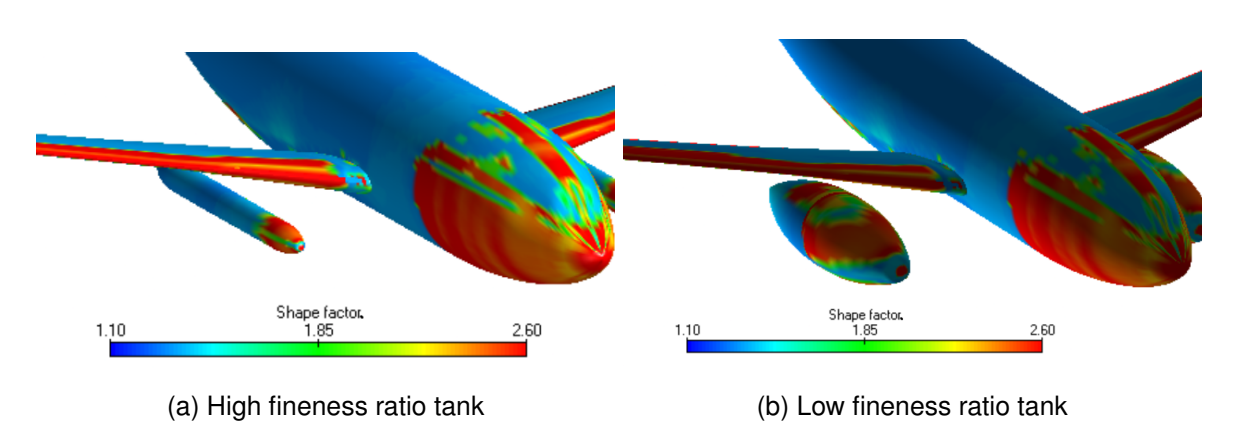


Figure 10 – Shape factor for a high and low fineness ratio tank

There is another factor which affects the large diameter tanks, when placed close to the wing root the tanks were seen to lower overall drag, this is represented by a negative interference drag. In general the behavior was only seen at 0.2 η , however in some cases it could be seen in positions as far as 0.6 η , though it should be noted that in those cases the drag improvement was believed to be within the margin of error of the solver, in addition, positioning a large tank towards the tip of the wing is a structurally questionable configuration. The large diameter tanks were seen to affect spanwise flows under the wings, the boundary layer thickness decreased on the outboard portion of the wing when a large tank was present near the root. This is thought to be why the 60 %MAC tanks show a decrease in interference drag at higher lengths. It should once again be noted that the tanks are modeled without pylons, more investigation is needed to see how this effect changes when a pylon is present.

For a transport aircraft drag must be minimized at cruise. To this end runs at an AoA of 0 and at Mach 0.75 are of interest. Only runs at a chordwise position of 0.3 will be considered. This position was chosen based on the discussion of Figure 8, as well as to ensure the tank is in a practical position from a structural point of view. In Figure 11 interference drag was plotted against vertical position at each spanwise position for four combinations of length and diameter. Runs that were structurally impractical, *i.e.* the large tanks at 0.8 η , were omitted. There's a clear trend of increasing interference drag with decreasing vertical separation. The relationship with spanwise position is less clear, though interference drag seems to increase with decreasing spanwise position. This trend is not seen however for the 60% MAC diameter, 350% MAC length tank at 0.2 η , as discussed before this tank behaves differently because of its effect on spanwise flows under the wing.

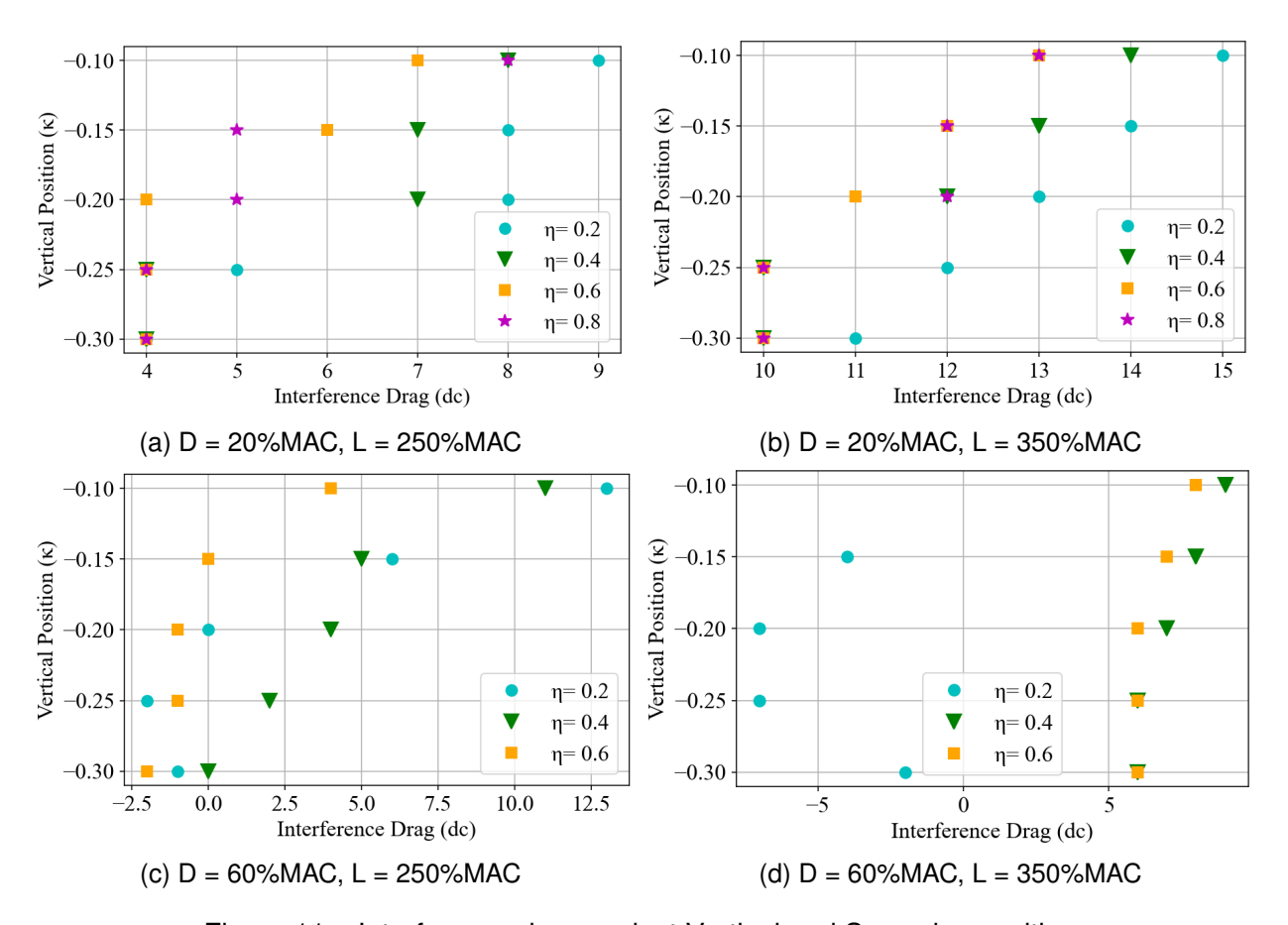


Figure 11 – Interference drag against Vertical and Spanwise position

3.2 Wing-Tank Interference Model

To determine a relationship between the tank-wing interference drag and tank parameters, a model was fit to the data. The model will only consider cruise conditions as they are of most interest to transport aircraft. The DLR-F6 is assumed to cruise at an AoA of 0° and at Mach 0.75, therefore only runs at that velocity and angle of attack will be used to fit the model. Runs with the largest tank size at 0.2 η will also be excluded. As discussed previously, in this case there's another factor affecting interference drag which does not seem to be present for all other test cases. In addition, the absolute value of the vertical position (κ) was used in the model. The model is based on an equation of the form:

$$C_{D interference} = k_1 \left(\frac{D}{c}\right)^{k_2} \left(\frac{L}{c}\right)^{k_3} \left(\frac{x}{c}\right)^{k_4} \left(\frac{y}{b/2}\right)^{k_5} \left(\frac{z}{c}\right)^{k_6} \tag{9}$$

The parameters (k_x) were found by a nonlinear least squares optimization. Such a method has been used by one of the authors in a previous work [17], where the correlation coefficients (k_x) are optimized to minimize the weighted sum of squares error according to Equation 10. Where y_i is the simulated value and \hat{y}_i is the value predicted by the coefficients, with weighting matrix (W) equal to the reciprocal of the variance of the data, summed for all N data points. The function is minimized using a Gauss-Newton line search approximation according to Equation 11, where the Hessian is approximated at each iteration as Equation 12.

$$f(x) = \frac{1}{2} \sum_{i=1}^{N} W_i (y_i - \hat{y}_i)^2$$

$$= \frac{1}{2} (y - \hat{y})^T W (y - \hat{y})$$

$$= \frac{1}{2} y^T W y - y^T W \hat{y} + \frac{1}{2} \hat{y}^T W \hat{y}$$
(10)

$$[J_x^T W J_x] p_x = -\nabla f(k_x) = -J_x^T W(y - \hat{y})$$
(11)

$$H = [J_x^T W J_x], \quad J_x = \frac{\partial \hat{y}}{\partial k}$$
 (12)

The model has an R^2 of 0.80. As expected the model shows interference drag increases with decreasing vertical position. The dependence on fineness ratio can also be seen, though as was observed in Figure 9, it is not directly dependent on fineness ratio, but rather a ratio of length to diameter with different powers. As chordwise position was previously shown not to be an important factor, the $(x/c)^{k_4}$ term was removed from the model. The change in R squared was very small, a decrease of 0.004. With chordwise position removed from the model, it shows a stronger, though still small, correlation with spanwise position. Given the weak correlation with spanwise position, the $\left(\frac{y}{b/2}\right)^{k_5}$ term was also removed from the model, the R^2 decreased to 0.76 as a result, with little change to other coefficients. The resultant coefficients for all three models are shown in Table 3. The resultant equation for the final model of interference drag between the wing and tank is seen in Equation 13.

Table 3 – Fitting Model Parameters

Parameter	Original Simplifie		Final	
$\phantom{aaaaaaaaaaaaaaaaaaaaaaaaaaaaaaaaaaa$	0.11	0.10	0.12	
k_2	-0.56	-0.54	-0.60	
k_3	2.56	2.53	2.51	
k_4	0.18	-	-	
k_5	-0.16	-0.20	-	
k_6	-0.38	-0.37	-0.32	
R^2	0.80	0.79	0.76	

$$C_{D \ interference} = 0.12 \left(\frac{(L/c)^{2.51}}{(D/c)^{0.6}} \right) \left(\left| \frac{z}{c} \right| \right)^{-0.32}$$
 (13)

The interference drag values predicted by the model were plotted against the simulated values in Figure 12, the line shows what would be expected if the model perfectly predicted the simulated values. In general the predicted values closely match the simulated values, with a residual standard deviation of 2.1 drag counts. Figure 13 investigates the statistical validity of the model. If the relative errors are normally distributed, minimizing the square of the error will result in a good correlation. To test if the errors are normally distributed, the relative error was determined for all N data points. They are then sorted, and assigned a rank from -N/2 to N/2. Using an inverse normal distribution, a deviation is determined for each error based on the ranking. For normally distributed data the plot of the deviation against the relative error will be a line with slope = 1 and intercept = 0. As shown in Figure 13, the data closely matches a normal distribution, this suggest that the model will be a good fit for the data.

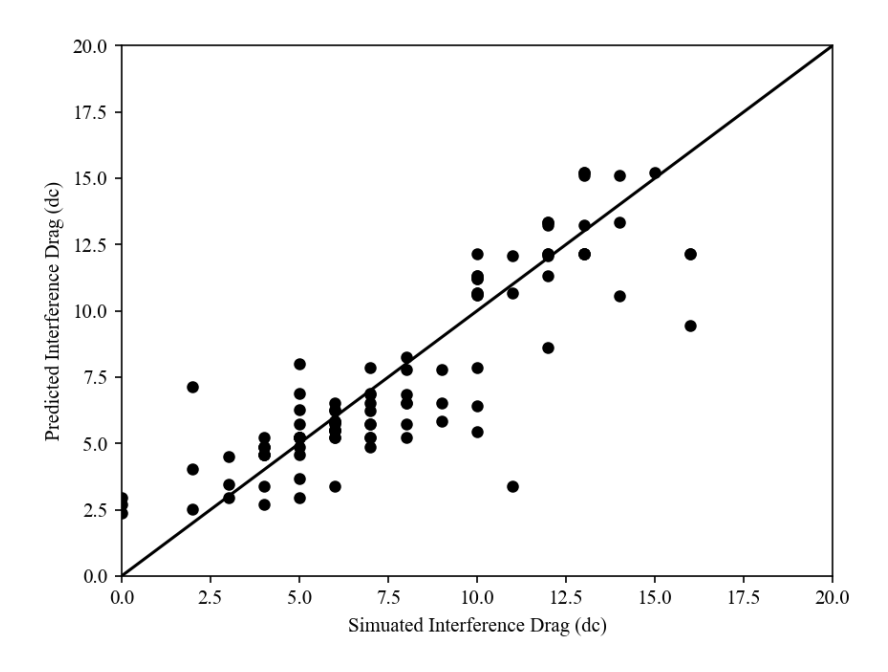


Figure 12 – Prediction error plot of the model

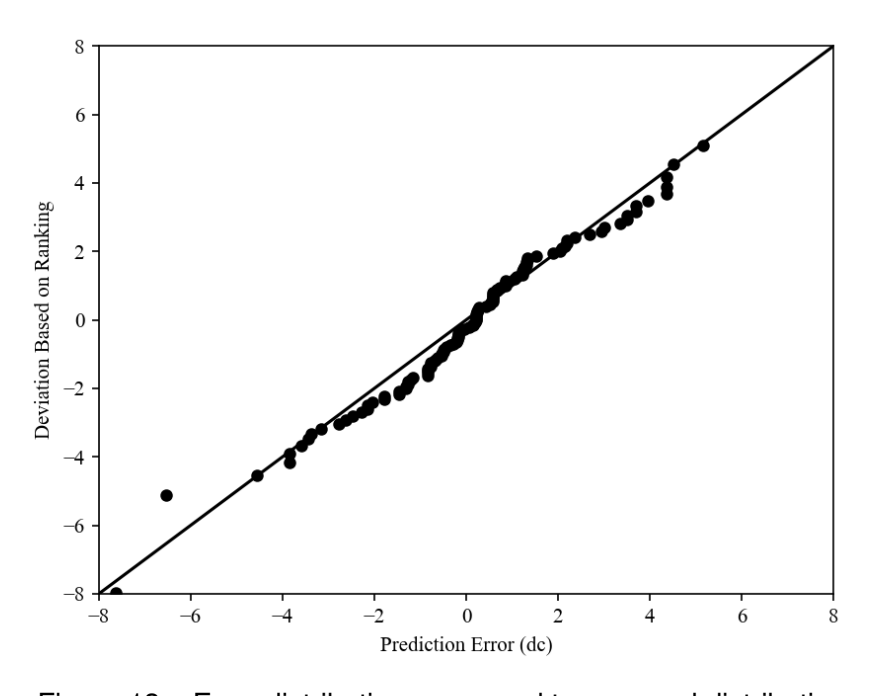


Figure 13 – Error distribution compared to a normal distribution

4. Conclusions

This paper investigates the interference drag for different configurations of external liquid hydrogen tanks with a representative transport aircraft, the DLR-F6. Analysis is performed using a flow solver which was validated against wind tunnel data. The trends are analyzed and a nonlinear regression is used to fit a model to the data. Results show a strong correlation with both length and fineness ratio as well as a weaker dependency on vertical separation. It was found that shorter, larger diameter tanks, with high vertical separations, reduced the interference drag caused by the tank-wing interaction by as much as 15 drag counts compared to long, small diameter tanks with low vertical separation. Results also suggest that with careful design of the tank size and position, overall drag could be reduced by altering spanwise flows under the wing, though more investigation is required to determine the feasibility and validity of such approach.

5. Contact Author(s) Email Address(es)

mailto: Ruben.Perez@rmc.ca, Caleb.Graham@rmc.ca

6. Acknowledgements

The authors gratefully thank Dr. Peter W. Jansen for his useful comments and suggestions during the preparation of this paper.

7. Copyright Statement

The authors confirm that they, and/or their company or organization, hold copyright on all of the original material included in this paper. The authors also confirm that they have obtained permission, from the copyright holder of any third party material included in this paper, to publish it as part of their paper. The authors confirm that they give permission, or have obtained permission from the copyright holder of this paper, for the publication and distribution of this paper as part of the ICAS proceedings or as individual off-prints from the proceedings.

References

- [1] Consolidated statement of continuing ICAO policies and practices related to environmental protection Climate change. Technical report.
- [2] Air TransportAction Group (ATAG). Waypoint 2050. In *Global Sustainable Aviation Forum*, September 2021.
- [3] Airbus. ZEROe Low Carbon Aviation, 2020.
- [4] Daniel Brewer. Hydrogen Aircraft Technology. CRC Press, 1991.
- [5] J. Brand, S. Sampath, and F. Shum. Potential Use of Hydrogen in Air Propulsion. In AIAA International Air and Space Symposium and Exposition: The Next 100 Years., 2003.
- [6] M. Gauss et al. Impact of H2O emissions from cryoplanes and kerosene aircraft on the atmosphere. *Journal of Geophysical Research*, 2003.
- [7] Airbus Deutschland GmbH et al. Liquid hydrogen fuelled aircraft system analysis. Technical Report GRD1-1999-10014, European Commission, 2003.
- [8] John L. Sloop. *Liquid Hydrogen as a Propulsion Fuel*. National Aeronautics and Space Administration, 1978.
- [9] Silberhorn et al. Assessment of hydrogen fuel tank integration at aircraft level. In *Deutscher Luft- und Raumfahrtkongress*, 2019.
- [10] Bryce Thomas, Ramesh K. Agarwal, and Christian V. Rice. Evaluation of sustainable transonic truss-braced wing aircraft configurations using liquid hydrogen fuel. In *AIAA SCITECH 2023 Forum*, 2023.
- [11] Stańkowski et al. Aerodynamics of aero-engine installation. Journal of Aerospace Engineering, 2016.
- [12] Logan King, Vivek Ahuja, and Roy Hartfield. Aerodynamic optimization of integrated wing-engine geometry using an unstructured vorticity solver. In *33rd AIAA Applied Aerodynamics Conference*, 2015.

- [13] G. Redeker. A selection of experimental test cases for the validation of cfd codes. Technical Report AGARD-AR-303, Adivsory Group for Aerospace Research and Development.
- [14] Gary Crowell. The descriptive geometry of nose cones. Technical report, Instituto de Física de São Carlos, 1996.
- [15] Vivek Ahuja. AERODYNAMIC LOADS OVER ARBITRARY BODIES BY METHOD OF INTEGRATED CIRCULATION. Doctoral dissertation, Auburn University, 2013.
- [16] Gregory M. Gatlin et al. Experimental investigation of the dlr-f6 transport configuration in the national transonic facility. In 2nd AIAA Drag Prediction Workshop, 2003.
- [17] Marc LaViolette and Ruben Perez. On the prediction of pollutant emission indices from gas turbine combustion chambers. In *ASME Turbo Expo 2012*, 2012.